Baran, Volodymyr; Senyshyn, Anatoliy; Karttunen, Antti J.; Fischer, Andreas; Scherer, Wolfgang; Raudaschl-Sieber, Gabriele; Fässler, Thomas F.

A Combined Metal-Halide/Metal Flux Synthetic Route towards Type-I Clathrates

Published in:
CHEMISTRY: A EUROPEAN JOURNAL

Published: 01/01/2014

Document Version
Peer-reviewed accepted author manuscript, also known as Final accepted manuscript or Post-print

Published under the following license:
Unspecified

Please cite the original version:
Baran, V., Senyshyn, A., Karttunen, A. J., Fischer, A., Scherer, W., Raudaschl-Sieber, G., & Fässler, T. F. (2014). A Combined Metal-Halide/Metal Flux Synthetic Route towards Type-I Clathrates: Crystal Structures and Thermoelectric Properties of A8Al8Si38 (A=K, Rb, and Cs). *CHEMISTRY: A EUROPEAN JOURNAL*, *20*, 15077-15088.

A combined metal-halide/metal flux syntheses route towards type-I clathrates – Crystal structures and thermoelectric properties of $A_8Al_8Si_{38}$ (A = K, Rb, and Cs)

Volodymyr Baran[a], Anatoliy Senyshyn[b], Antti J. Karttunen[c], Andreas Fischer[d], Wolfgang Scherer[d], Gabriele Raudaschl-Sieber[a], Thomas. F. Fässler*[a].

[a] Department Chemie, Technische Universität München, Lichtenbergstraße 4, 85747 Garching b. München, Germany

[b] Forschungsneutronenquelle Heinz Maier-Leibnitz FRM-II, Technische Universität München, Lichtenbergstrasse 1, 85747 Garching b. München, Germany

[c] Department of Chemistry, Aalto University, FI-00076 Aalto, Finland

[d] University of Augsburg, Institute of Physics, 86159 Augsburg, Germany

* Corresponding author

Supporting information for this article is available on the WWW under http://www.chemeurj.org/ or from the author.

Abstract: Single phase samples of the compounds $K_8Al_8Si_{38}$ (**1**), $Rb_8Al_8Si_{38}$ (**2**) and $C_{7.9}Al_{7.9}Si_{38.1}$ (**3**) were obtained with a high crystallinity and good quantities using a novel flux method using two different flux materials such as Al and the respective alkali-metal halide salt KBr, RbCl and CsCl. We found that this approach facilitates removing the product mixture from the container and also allows a convenient extrusion of the flux media due to the good solubility of the halide salts in water. The products were analyzed by means of single crystal X-ray structure determination, powder X-ray and neutron diffraction experiments, ^{27}Al-MAS NMR measurements, quantum chemical calculations, as well as magnetic and transport measurements (thermal conductivity, electrical resistivity and Seebeck coefficient). Due to the excellent quality of the neutron diffraction data, the difference between the nuclear scattering factors of silicon and aluminum atoms was sufficient to refine their mixed occupancy at specific sites. The role of variable range hopping for the interpretation of the resistivity as well as the Seebeck coefficient is discussed.

Keywords: clathrates, thermoelectrics, Zintl phases, transport properties, neutron powder diffraction

Introduction

Ever since the first crystal structure of an intermetallic clathrate was described in 1965 by J. Kasper *et al.* [1] the chemistry of clathrates has received an enormous rush. A relatively low thermal conductivity and a high electrical conductivity of some intermetallic clathrates[2] identify them as promising materials for thermoelectric applications. For example, a maximum value of the dimensionless figure of merit ZT = 1.35 was reached for $Ba_8Ga_{16}Ge_{30}$ at 900 K,[3] albeit other values have also been reported.[4] For n-doped $Ba_8Ga_{16}Sn_{30}$ the highest value of the figure of merit (1.45) is reported at 500 K.[5] In the meanwhile, many new representatives of group

14 intermetallic clathrates of known types have been found[6] and completely new types of clathrates have recently been suggested.[7] Furthermore, it has been shown that structure diversities such as defects and superstructures might influence on the electrical properties.[8] Accordingly, the investigation and development of efficient synthesis methods remains an important aspect in the research area of intermetallic clathrates.

Methods for the preparation of clathrates differ substantially on the chemical nature of the elements forming the clathrate network. Almost all intermetallic clathrates contain one of the group 14 elements (Si, Ge, Sn) and the synthetic path depends on their reactivity. Due to its high melting point, silicon is the most inert element during high temperature reactions yielding clathrates. Heating the respective elements above their melting point and subsequent annealing is a common procedure for the synthesis of silicon containing clathrates. This synthetic path facilitates also the production of ternary or quaternary clathrates.[9] Other methods include preceding arc melting and annealing as described for $K_7B_7Si_{39}$.[10] In some cases crystalline products can be obtained directly from the arc melting procedure as it has been shown for $Ba_8Cu_4Si_{42}$.[11] Other routes apply heating of the sample to the rather high temperature (up to 1700 K) using high-frequency furnaces as it has been employed for the transition metal containing clathrates $Ba_8M_xSi_{46-x}$.[12] It should be mentioned that high temperature routes for the reaction of the elements limit the choice of suitable containers. Thus, glassy carbon, tantalum or alumina crucibles are required for synthesis of anionic clathrates from elements or more reactive binary precursors (especially with alkali metals).

Another sophisticated method for the synthesis of Si-based clathrates relies on the usage of more reactive precursors instead of the pure elements (especially with alkali metals).[13] Decomposition of the binary silicides *A*Si (*A* = Na, K, Rb) results in A_xSi_{46} or A_xSi_{136} depending on the reaction conditions and it is usually performed in vacuum ~~atmosphere~~ at temperatures between 600 and 900 K. Similarly, ternary silicon clathrates such as $Na_{16}Ba_8Si_{136}$ were obtained by thermal decomposition of Na_2BaSi_4 at 623 K.[14] A new variation of this method is the slow removal of alkali metal vapor from an alkali-silicide precursor placed between spatially separated graphite plates in a closed volume under uniaxial pressure.[15] This route allows to selectively synthesize type-I or type-II clathrates single-crystals.

High-pressure and high-temperature (HPHT) syntheses are used for preparation of Si-based clathrates as well. For instance, $Cs_{8-x}Si_{46}$ was obtained from mixtures of Cs_4Si_4 and α-Si at HPHT conditions.[16] A new variation of the high-pressure synthesis is the spark-plasma-sintering (SPS) technique which has been used to synthesize of clathrates of various compositions.[17] Another approach for the preparation of Ba-Al-Si clathrates and the formation of large single crystals is the Al flux method.[18]

Recently, also preparation methods that use ~~oxidants~~ oxidizing agents have been introduced to obtain clathrates. For example, the oxidation of Na_2BaSi_4 by gaseous HCl leads to formation of the $Na_2Ba_6Si_{46}$[19] whereas gaseous HCl or H_2O react with NaSi or KSi yielding the respective clathrate-I compounds.[20] For the synthesis of germanium clathrates, lower temperatures are sufficient. Many clathrates have been prepared by direct annealing of the elements under vacuum or under inert gas atmosphere or by arc melting.[21] At the same time, a route with the Zintl phase K_4Ge_9 as precursor has been realized for the formation of the clathrate-I structure $K_4Hg_{3+x}Ge_{46-x}$ in presence of Hg or HgO.[22] Since tin has an even lower melting point than Si and Ge, Sn-based clathrates usually are synthesized by annealing of a stoichiometric mixture of the elements without any preliminary preparation.[8b, 23]

In this paper we report a new synthesis route based on a combination of arc-melting, ball-milling and flux synthesis methods that result in the formation of type-I clathrates $K_8Al_8Si_8$ (**1**), $Rb_8Al_8Si_{38}$ (**2**) and $C_{7.9}Al_{7.9}Si_{38.1}$

(**3**) as single phase materials in large quantities. The structures were investigated using X-ray and neutron powder diffraction methods as well as single crystal X-ray structure determination. Thermoelectric measurements were performed for all reported clathrates.

Results

The compounds $K_8Al_8Si_{38}$ (**1**), $Rb_8Al_8Si_{38}$ (**2**) and $C_{7.9}Al_{7.9}Si_{38.1}$ (**3**) were obtained as highly crystalline, single phase materials (**2** and **3** contain very small amounts of the eutectic $Al_{1-x}Si_x$ which was only visible by neutron scattering) using a flux method in alumina crucibles. The novel combined approach uses two different flux materials such as Al and the respective alkali-metal halide salt. We found that the combination of the metals and metal salt flux media allows an easier removal of the product mixture from the container and also ~~allows~~ leads to a convenient extraction of the flux media due to the good solubility of halide salts in water.

The analysis of the products by X-ray powder diffraction and neutron diffraction methods shows the presence of primitive cubic cells indicative for clathrate-I structure type of compounds **1** to **3**, respectively (Figure 1). Superstructure reflections were observed neither for powdered samples nor for the single crystals (see below). The parameter of the cubic unit cells for clathrates **1**, **2** and **3** were determined ~~with WinPLOTR~~ using FullProf [24] and are given in Table 1. ~~In addition~~ The unit cell parameters were determined also from neutron powder and X-ray single crystal data. As expected, we observe an enlargement of the lattice parameters with increasing the size of the guest atoms *A*.

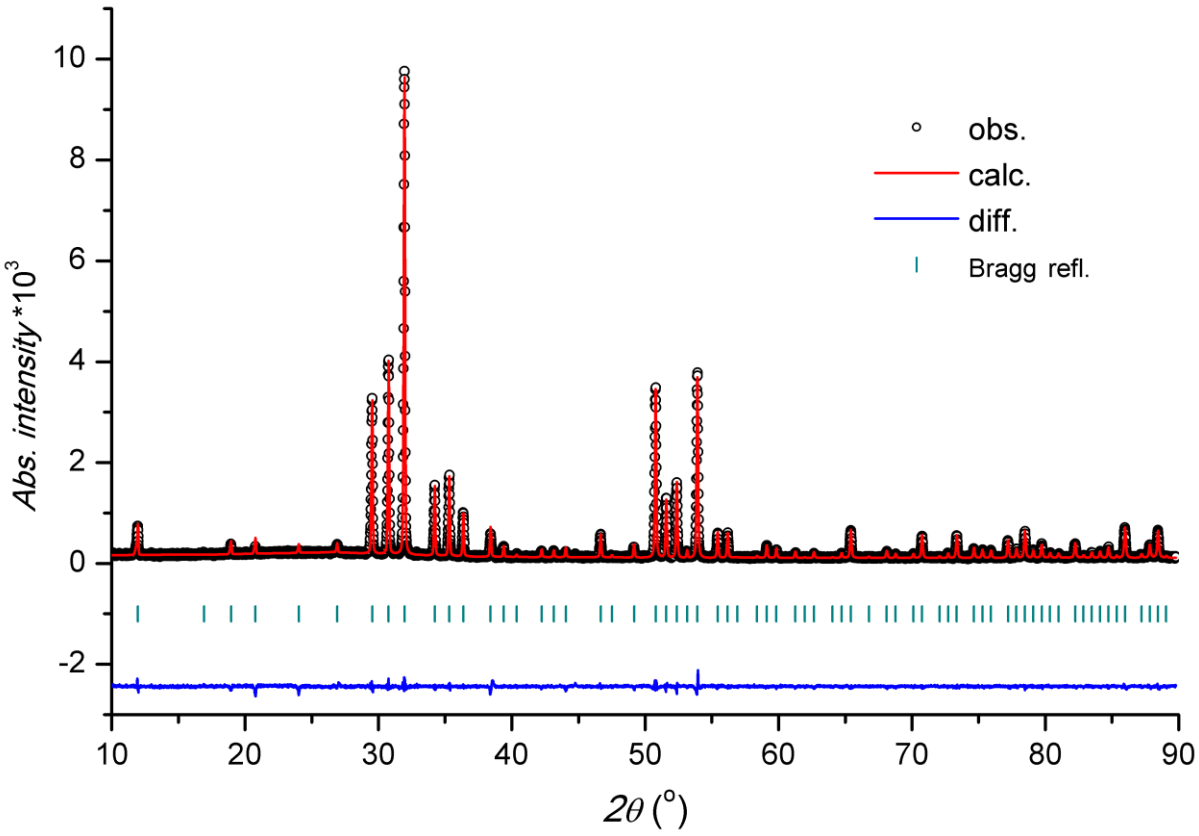

Figure 1. X-ray powder diffraction pattern and Rietveld plots for $K_8Al_8Si_{38}$. Corresponding plots for $Rb_8Al_8Si_{38}$ and $C_{7.9}Al_{7.9}Si_{38.1}$ are given in Supporting Information (Figure S1).

The unit cell of the clathrate type-I structures contains 54 atoms (space group *Pm-3n*, Z=1) of which 46 atoms are located at Wyckoff positions 6*c*, 16*i* and 24*k*, ~~which~~ and build the clathrate host framework and eight guest atoms at Wyckoff positions 2*a* and 6*d*. The framework of four-bonded host atoms provides two types of polyhedra that encapsulate the alkali metal guest atoms: the smaller polyhedron is a 20-atom pentagonal dodecahedron [5^{12}] and the bigger one is a 24-atom tetrakaidecahedron [$5^{12}6^2$]. The [5^{12}] and [$5^{12}6^2$] cages are occupied by the guest atoms at positions 2*a* and 6*d*, respectively. Clathrate-I compounds are known as electron-precise semiconducting Zintl phases [25] but also as electron deficient or electron rich metals. Electron ~~accurate~~ precise valence compounds with a full occupation of the guest atom sites by alkali metals *A* require the substitution of the same number of tetrel (*Tt*) by triel (*Tr)* elements in the framework. The formal transfer of the valence electrons from the *A* atoms to the *Tr* element leads to the situation in which all framework atoms possess four valence electrons to form four covalent bonds For the heavier homologues of Si the host structure can also form vacancies resulting in three-bonded frame work atoms that can uptake additional electrons and form lone pairs such as in the binary phases $A_8Ge_{44}\square_2$.[6, 26]

Table 1. Comparison of unit cell parameters

Empirical formula	$K_8Al_8Si_{38}$	$Rb_8Al_8Si_{38}$	$C_{7.9}Al_{7.9}Si_{38.1}$
neutron (powder)	10.48914(6)	10.53163(7)	10.58734(7)
X-ray (powder)	10.4886(6)	10.53069(1)	10.5848(4)
X-ray (single crystal)	10.470(1)	10.517(1)	10.569(1)

The present ternary compounds $A_8Al_8Si_{38}$ correspond to valence compounds according to $(A^+)_8[(Al^-)_8Si_{38}]$. An EDX analysis of selected single crystals confirms the composition as determined by the crystallographic data: $K_{7.6(4)}Al_{7.8(3)}Si_{38.6(5)}$, $Rb_{7.2(1)}Al_{8.1(3)}Si_{38.6(2)}$, and $Cs_{7.9(7)}Al_{8.5(9)}Si_{37.6(9)}$ (Table S5, for crystallographic composition see Table S1).

In order to determine the ratio of Al and Si at the various host atom positions, we collected neutron powder diffraction and X-ray single crystal data. Due to the difference of only one electron between Al and Si atoms the X-ray scattering power is rather similar (8% difference at ~~θ~~ Q= 0°) and also the nuclear scattering form factors of Al and Si differ only slightly (20% difference). Due to the excellent data quality of the neutron diffraction data the difference between the individual scatter factors was sufficient to refine the mixed occupancy of Si and Al at specific sites.

For **2** and **3** Rietveld refinement of neutron powder diffraction data reveals the atomic ratio A:Al:Si = 8:8:38 (Table 2). For **1** the overall composition was fixed to 8:8:38 because of an uncertainty due to small amounts of impurities Si and $Al_{1-x}Si_x$. The site occupation factors of the free refinement of X-ray single crystal data are listed in Table S1 (full discussion of the single crystal X-ray data and structure analysis are given in Supporting Information). Based on the X-ray single crystal data the composition differs from 8 : 8 : 38 since for **1**, **2** and **3** the following stoichiometric compositions were derived: $K_8Al_{6.5}Si_{39.5}$, $Rb_8Al_{11}Si_{35}$ and $Cs_{7.9}Al_{10.2}Si_{35.8}$, respectively. In case of **2** and **3** the total Al content appears to be higher than that of **1**, however, the refinements were biased by convergence problems. The previously reported structure data of $K_8Al_8Si_{38}$, which had been obtained from X-ray diffraction data only[27] are consistent with the neutron powder data reported here. It should be noted that we collect X-ray data at room temperature (Table 3). Since the scattering powers of Al and Si are rather similar with respect to X-ray radiation we applied the structure models with the Al and Si ratio as obtained from the neutron data also for the single crystal X-ray data refinement. Carful inspection of the single crystal X-ray data and powder neutron data of clathrate **3** shows in contrast to **1** and **2** that the 2*a* atomic site is not fully occupied with Cs (s.o.f.(Cs1)=0.94(1)). Attempts to simultaneously refine the Cs1/Al/Si ratio failed. Therefore we fixed the Cs/Al/Si ratio based on the Cs content to an electron precise Zintl phase $Cs_{7.9}Al_{7.9}Si_{38.1}$ fully in accordance to the measured semiconducting property of **3**. We have further tried to simultaneously refine powder neutron data and the single crystal X-ray data, which however did not lead to any significant improvement of the model.

Table 2. Crystallographic data of $K_8Al_8Si_{38}$ (**1**) $Rb_8Al_8Si_{38}$ (**2**) and $C_{7.9}Al_{7.9}Si_{38.1}$ (**3**) (Rietveld refinement based on neutron powder data)

	1	**2**	**3**
refined formula	$K_8Al_{8.02(9)}Si_{37.98(9)}$	$Rb_8Al_{8.01(17)}Si_{37.99(17)}$	$Cs_{7.89(1)}Al_{7.90(11)}Si_{38.10(11)}$
space group	~~*Pm-3n*~~	*Pm-3n*	~~*Pm-3n*~~
unit cell dimension (Å)	10.48914 (6)	10.53163(7)	10.58734(7)
V(Å^3)	1154.036(12)	1168.119(13)	1186.746(15)
wavelength (Å)	~~1.54832~~	1.54832	~~1.54832~~
step scan increment (2θ)	~~0.05~~	0.05	~~0.05~~
2θ range (deg)	0.95 – 151.9	2 – 156	2 – 155.9
program	~~*FullProf*~~	*FullProf*	~~*FullProf*~~
zero point (2θ)	-0.0431(11)	0.0267(11)	0.0459(12)
profile points	3020	3079	3849
shape parameter	η = 0.191 (6)	η = 0.113(4)	η = 0.095(4)
Caglioti parameters	U = 0.035(1)	U = 0.056(1)	U = 0.071(2)
	V = -0.042(2)	V = -0.077(2)	V = -0.072(3)
	W = 0.120 (1)	W = 0.138 (1)	W = 0. 134(1)
No. of reflections	252	258	264
No. of refined parameters	70	35	39
R_F	1.74	2.20	2.93
R_B	2.05	3.34	4.02
R_P	5.70	6.02	6.60
R_{exp}	2.41	1.87	1.87
R_{wp}	4.94	5.09	6.12
χ^2	4.20	7.40	10.75

Table 3. Crystallographic data and parameters of the structure refinement for $K_8Al_8Si_{38}$ (**1**), $Rb_8Al_8Si_{38}$ (**2**) and $C_{7.9}Al_{7.9}Si_{38.1}$ (**3**) (single crystal X-ray diffraction; the Al/Si occupation ratio taken from neutron powder data)

	1	**2**	**3**
formula (weight/g mol^{-1})	1596.06	1967.02	2333.36
T (K)	293(2)	296(2)	293(2)
Diffractometer	APEX II	APEX II	APEX II
wavelength (Å)	0.71073	0.71073	0.71073
space group	*Pm-3n*	*Pm-3n*	*Pm-3n*
Z	1	1	1
unit cell dimension (*a*/Å)[a]	10.4886(6)	10.53069(17)	10.5848(4)
V (Å^3)	1153.86(11)	1167.81(3	1185.90(8)
$\rho_{calcd.}$ (g cm^{-3})	2.297	2.797	3.267
crystal size (mm^3)	0.05×0.1×0.1	0.1×0.1×0.1	0.1×0.1×0.1
µ. (mm^{-1})	1.908	9.455	7.131
F(000)	788	932	1071
Θ range (deg)	2.75 – 45.36	2.74 – 45.26	2.72 – 40.23
R_{int}	0.0319	0.0419	0.0264
R_{sigma}	0.0042	0.0050	0.0040
reflections collected	159604	154369	104377
independent reflections	907	912	703
reflection with [$I > 2\sigma(I)$]	850	865	697
data/restrains/parameter	907/0/15	912/0/15	703/0/16
goodness-of-fit on F^2	1.148	1.239	1.550
weighting parameters[b]	0.0139 0.1080	0.0085 0.2194	0.0048 0.4376
final R indexes [$I > 2\sigma(I)$]	R_1= 0.0081,	R_1= 0.0103,	R_1= 0.0089,
	wR_2= 0.0236	wR_2= 0.0252	wR_2= 0.0224
R indexes (all data)	R_1= 0.0096,	R_1= 0.0118,	R_1= 0.0090,
	wR_2= 0.0246	wR_2= 0.0256	wR_2= 0.0224
largest diff. peak and hole (e Å^{-3})	0.22, -0.31	0.50, -1.19	0.26, -0.53

[a] data taken from powder X-ray diffraction

[b] $w = 1/\ \sigma^2\ F_o^2\ +\ aP\ ^2 + bP$ where $P = (F_o^2 - F_c^2)/3$

The crystallographic data for compound **1**, **2** and **3** obtained from neutron powder data (NPD) are listed in Table 4. The Al distribution in the host structure depends on the guest atoms. The most significant changes occur at the 6*c* position: the Al content at 6*c* decreases from K to Cs. For the 16*i* atomic position the Al content for **1** and **2** is rather similar and low, but higher for **3**. In case of the 24*k* position we have a slight increase of the Al content from **1** to **2** and almost equal to **3**.

The analysis of the interatomic distances (Table 5) shows a dependence on the type of the guest atom: since the atomic radius of the guest atoms increases from K to Cs, the unit cell and thus the interatomic distances increase. The distances Si3/Al3-Si3/Al3 increase from 2.4501 to 2.5363 Å and Si2/Al2-Si3/Al3 from 2.4077 to 2.4269 Å, whereas the distance between Si1/Al1-Si3/Al3 slightly increase from 2.4908 to 2.4950 Å and Si2/Al2-Si2/Al2 slightly decrease from 2.3905 to 2.3835 Å but are virtually unaffected. Notice the most significant change occurs for Si3/Al3-Si3/Al3 and Si2/Al2-Si3/Al3 that are part of the smaller [5^{12}] cage. The size of the guest atom has a stronger impact on bond length changes between the host atoms as it is also indicated by the *A* – Tt/Tr distance in the smaller [5^{12}] cage that are in the range of 3.3467-3.4102 Å, 3.3672-3.4321 Å and 3.3927-3.4553 Å for **1, 2** and **3**, respectively. Whereas for the larger [$5^{12}6^2$] cage the distances are considerable longer and are in the range of 3.5537-4.0584 Å for clathrate **1**, 3.5731-4.0578 Å for **2** and 3.5969-4.0653 Å for **3**. The same suggestion has been proposed before.[7] The anisotropic displacement parameters follow the known trend that the atoms that are located in the larger voids (*A*2) possess larger ADPs than on *A*1 position. Whereas the ADPs decrease with increasing mass of the *A* atoms in the larger voids due to the decreasing rattling of the heavier atoms.

Table 4. Atomic coordinates and isotropic atomic displacement for $K_8Al_8Si_{38}$, $Rb_8Al_8Si_{38}$ and $C_{7.9}Al_{7.9}Si_{38.1}$ (neutron powder data).

Atom	Site	*x/a*	*y/b*	*z/c*	s.o.f.	U_{eq}, Å^2
$K_8Al_8Si_{38}$ (**1**)						
K1	2*a*	0	0	0	1	0.0093(4)
K2	6*d*	¼	½	0	1	0.0223(6)
Si1/Al1	6*c*	¼	0	½	0.25(3)/0.75(3)	0.0070(5)
Si2/Al2	16*i*	0.18421(3)	*x*	*x*	0.96(1)/0.04 (1)	0.0063(2)
Si3/Al3	24*k*	0	0.30342(6)	0.11679(5)	0.88 (1)/0.12(1)	0.0059(3)
$Rb_8Al_8Si_{38}$ (**2**)						
Rb1	2*a*	0	0	0	1	0.0108(3)
Rb2	6*d*	¼	½	0	1	0.0207(3)
Si1/Al1	6*c*	¼	0	½	0.40(4)/0.60(4)	0.0107(6)
Si2/Al2	16*i*	0.18459(4)	*x*	*x*	0.95(3)/0.05(3)	0.0086(2)
Si3/Al3	24*k*	0	0.30360(6)	0.11845 (5)	0.85(2)/0.15(2)	0.0086(3)
$Cs_8Al_8Si_{38}$ (**3**)						
Cs1	2*a*	0	0	0	0.949(7)	0.0091(5)
Cs2	6*d*	¼	½	0	1	0.0152(4)
Si1/Al1	6*c*	¼	0	½	0.59(3)/0.41(3)	0.0122(6)
Si2/Al2	16*i*	0.18501(3)	*x*	*x*	0.90(2)/0.10(2)	0.0080(2)
Si3/Al3	24*k*	0	0.30359(5)	0.11978(5)	0.84(1)/0.16(1)	0.0088(3)

Table 5 Bond lengths (Å) based on neutron powder diffraction data.

$K_8Al_8Si_{38}$ (**1**)				$Rb_8Al_8Si_{38}$ (**2**)				$C_{7.9}Al_{7.9}Si_{38.1}$ (**3**)			
atom pairs			d/Å	atom pair			d/Å	atom pair			d/Å
Si1/Al1	Si3/Al3	×4	2.4908(4)	Si1/Al1	Si3/Al3	×4	2.4895(4)	Si1/Al1	Si3/Al3	×4	2.4950(5)
Si2/Al2	Si2/Al2		2.3905(4)	Si2/Al2	Si2/Al2		2.3863(6)	Si2/Al2	Si2/Al2		2.3835(6)
	Si3/Al3	×3	2.4077(7)		Si3/Al3	×3	2.4157(4)		Si3/Al3	×3	2.4269(7)
Si3/Al3	Si3/Al3		2.4501(7)	Si3/Al3	Si3/Al3		2.4949(1)	Si3/Al3	Si3/Al3		2.5363(7)
K1	Si2/Al2	×8	3.3467(3)	Rb1	Si2/Al2	×8	3.3672(4)	Cs1	Si2/Al2	×8	3.3927(4)
	Si3/Al3	×12	3.4102(6)		Si3/Al3	×12	3.4321(2)		Si3/Al3	×12	3.4553(6)
K2	Si3/Al3	×8	3.5537(4)	Rb2	Si3/Al3	×8	3.5731(6)	Cs2	Si3/Al3	×8	3.5969(4)
	Si1/Al1	×4	3.7085(0)		Si1/Al1	×4	3.7235(1)		Si1/Al1	×4	3.7432(0)
	Si2/Al2	×8	3.8963(3)		Si2/Al2	×8	3.9100(4)		Si2/Al2	×8	3.9283(4)
	Si3/Al3	×4	4.0584(5)		Si3/Al3	×4	4.0578(1)		Si3/Al3	×4	4.0653(5)

Table 6 lists the anisotropic atomic displacement parameters (ADPs) for the compounds **1**, **2** and **3**. All atomic displacement parameters for the host atoms show almost isotropic behavior. As expected, the atomic displacement parameters for the guest atom at the 2*a* Wyckoff site inside the smaller [5^{12}] cage are almost isotropic (Fig. 2), whereas a larger anisotropy is observed for the guest atom at 6*d* Wyckoff site located in the larger [$5^{12}6^2$] cage. The value U_{11} is about half the value of the U_{22}=U_{33} for **1** and decreases from **1** to **3** (Table 6). The ratio $U_{22}(2a)/U_{22}(6d)$ is approximately 2.9 for **1**, 2.2 for **2** and 1.8 for **3**.

The ADPs obtained from the single crystal data (Table S3) show in general similar results if compared to the neutron powder data. A small discrepancy appears due to the different methods. In both data sets the host atoms show almost isotropic behavior with somewhat larger ADPs for the 6*c* compared to 24*k* and 16*i*. This correlates with the highest aluminum content at the 6*c* site. For the single crystal data the ADPs of the guest atoms inside the smaller [5^{12}] cage decrease, as expected from the increasing the mass of the atoms. For the guest atom located in the larger [$5^{12}6^2$] cage, ADPs show slightly larger values of the anisotropy but similar to the results from the neutron experiment.

Table 6. Anisotropic displacement parameters for **1**, **2** and **3** (neutron powder data)

Atom	Site	U_{11}	U_{22}	U_{33}	U_{12}	U_{13}	U_{23}
	$K_8Al_8Si_{38}$ **(1)**						
K1	2*a*	0.0093(4)	U_{11}	U_{11}	□	□	□
K2	6*d*	0.0139(7)	0.0266(6)	U_{22}	□	□	□
Si1/Al1	6*c*	0.0089(6)	0.0060(5)	U_{22}	□	□	□
Si2/Al2	16*i*	0.0063(2)	U_{11}	U_{11}	0.0003(2)	U_{12}	U_{12}
Si3/Al3	24*k*	0.0059(3)	0.0063(3)	0.0055(3)	□	□	0.0003(2)
	$Rb_8Al_8Si_{38}$ **(2)**						
Rb1	2*a*	0.0108(3)	U_{11}	U_{11}	□	□	□

Rb2	6*d*	0.0150(4)	0.0236(3)	U_{22}	□	□	□
Si1/Al1	6*c*	0.0103(7)	0.0109(6)	U_{22}	□	□	□
Si2/Al2	16*i*	0.0086(2)	U_{11}	U_{11}	0.0001(2)	U_{12}	U_{12}
Si3/Al3	24*k*	0.0091(3)	0.0077(3)	0.0091(3)	□	□	0.0003(3)
	$C_{7.9}Al_{7.9}Si_{38.1}$ **(3)**						
Cs1	2*a*	0.0091(5)	U_{11}	U_{11}	□	□	□
Cs2	6*d*	0.0124(5)	0.0166(3)	U_{22}	□	□	□
Si1/Al1	6*c*	0.0114(7)	0.0126(5)	U_{22}	□	□	□
Si2/Al2	16*i*	0.0080(2)	U_{11}	U_{11}	-0.0003(2)	U_{12}	U_{12}
Si3/Al3	24*k*	0.0080(3)	0.0086(3)	0.0098(3)	□	□	0.0001(3)

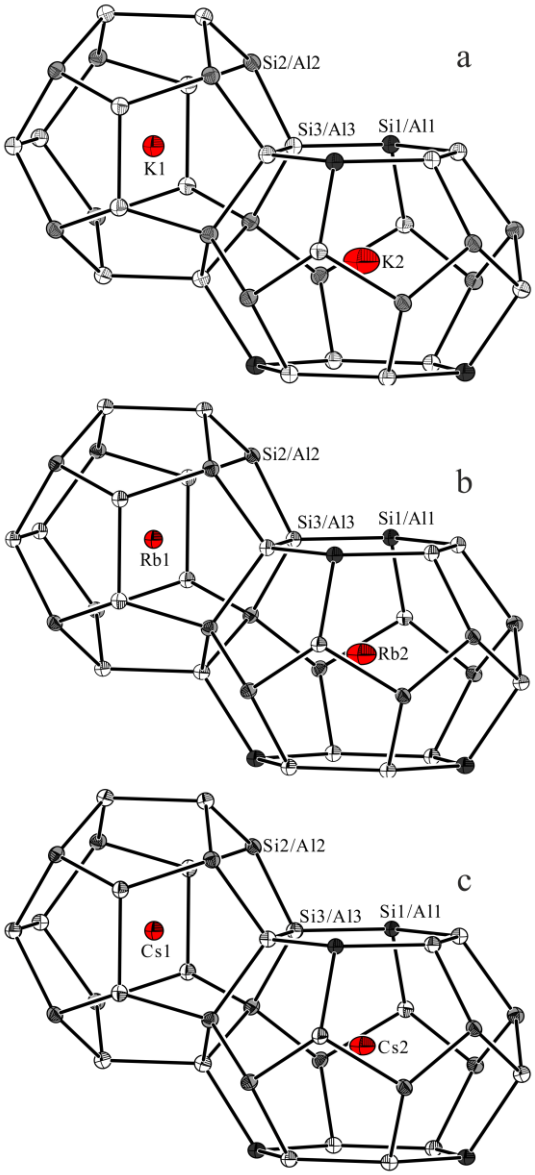

Figure 2 Partial structure of clathrates. (a) $K_8Al_8Si_{38}$, (b) $Rb_8Al_8Si_{38}$, (c) $C_{7.9}Al_{7.9}Si_{38.1}$. The alkali metal, mixed positions 6*c*, 16*i* and 24*k* are drawn as red, dark grey, grey, and white ellipsoids, respectively. All thermal ellipsoids are presented at 90% probability from X-ray data.

Figure 3 shows the section from 0 to 500 ppm of the ^{27}Al-MAS NMR spectrum for $K_8Al_8Si_{38}$, $Rb_8Al_8Si_{38}$ and $C_{7.9}Al_{7.9}Si_{38.1}$, respectively. The full spectra are presented in Supp. Inf. (Figure S6). A symmetric signal at approximately 1640 ppm (not shown in Figure 3) shows rotational side bands and is attributed to Al metal[28] as part of the Al/Si eutectic mixture which has also been observed in the neutron powder diffraction diagram of all samples. The presence of Al/Si eutectic is also indicated by the thermal investigations showing an endothermic peak at about 845 K.[29]

The signals at ≈180 ppm and ≈270 ppm show a Knight shift, indicating that the Al atoms in the framework are interacting with the conduction electrons.

The signals in the range between 120 and 350 ppm are assigned to $A_8Al_8Si_{38}$ since they are shifted to lower frequencies if compared to elemental Al.[30] A line shape analysis indicates that those signals are composed by several contributions. In the case of $K_8Al_8Si_{38}$ (Figure 3a) a strong signal at 188 ppm and two broad, but overlapping signals at 275 and 315 ppm are present. For $Rb_8Al_8Si_{38}$ again one sharp signal at 186 ppm is observed but two broad resonances are merged under the broad asymmetric signal at 278 ppm as indicated also by the high frequency shoulder (Figure 3b). Finally one signal with narrow width at 180 ppm and a broad signal at 269 ppm is present in the case of $C_{7.9}Al_{7.9}Si_{38.1}$. The range of region where we observe signals is in good agreement with results presented by Condron *et al.* [18b, 18d]

For the integration of the three main signals (without rotating sidebands) the signals with a small difference in chemical shift were treated as merged. The integration leads the ratios for the low to high filed signals of 2.17: 1.07 for **1**, and 1.53: 1.14for **2**, and 7.66: 8.68 for **3**. Due to rather similar chemical environment of the atoms at 24*k* and 16*i* atomic sites (see discussion above) the signals of the broad peak were assigned to Al2 and Al3. The results reveal a higher Al content at the 6*c* compared to the Al2 and Al3 position which is in agreement with the crystallographic data (see Supporting Information).

We also carried out first-principles NMR calculations at the DFT-PBE-GIPAW level to interpret the experimental NMR spectra (see Experimental for computational details). The atomistic calculations are carried out with explicit Si and Al framework atoms instead of mixed Si/Al sites, so we first investigated various ordered structural models for the distribution of the Al atoms in the Si–Al framework. The eight Al atoms could in principle be distributed in numerous ways within the 46-atom framework, but in practice the experimentally determined site occupancy factors and the well-known site-occupancy guidelines for type I-clathrates greatly reduce the number of reasonable structural models.[31] The key guideline in constructing the models for Al distribution is to minimize the number of Al–Al bonds. In building the structural models, we applied the primitive cubic unit cell with 46 framework atoms (space group *P*1) since larger supercells would have rendered the NMR calculations unfeasible. The Al site occupancies resulting for the applied structural models are in line with the experimental occupancies. The total numbers of Al atoms on the 6*c*/16*i*/24*k* sites of **1**, **2**, and **3** are 5/1/2, 4/1/3, and 3/2/3, respectively. In terms of site occupancy factors this corresponds to 0.83/0.06/0.08 for **1** [exp. 0.75(3)/0.04(1)/0.12(1)], 0.67/0.06/0.13 for **2** [exp. 0.60(4)/0.05(3)/0.15(2)], and 0.50/0.13/0.13 for **3** [exp. 0.41(3)/0.10(2)/0.16(1)]. Total energy calculations for the derived structural models showed the energy differences between the energetically most favorable isomers to be very small. For example, the energy difference between the two lowest energy isomers is only 6, 2, and 8 kJ/mol for **1**, **2**, and **3**, respectively, which is very well in line with similar structural studies on Ba–Ga–Ge clathrates.[32] We did not re-optimize the experimental atomic positions for our structural models since the optimization would bring the structure to a local minimum which can then be somewhat different from the "average" experimental structure with truly

mixed-occupations that is probed in the NMR studies. The unit cell coordinates for the final structural models used for the NMR calculations are listed in the Supporting Information.

For the discussion of the ^{27}Al NMR spectrum in the 0–500 ppm range, we averaged the NMR chemical shifts (δ_{iso}) calculated for all Al atoms within each crystallographic site. For example, the ^{27}Al δ_{iso} for the five 6*c* Al atoms in **1** are 189, 184, 184, 195, and 190 ppm and for our discussion we use the average δ_{iso} of 188 ppm. The calculated δ_{iso} for **1**, **2**, and **3** provide a straightforward interpretation of the experimental ^{27}Al NMR spectra. The narrowest signal observed at 170-190 ppm corresponds to the 6*c* site, which has theoretical δ_{iso} of 188, 186, and 177 ppm for **1**, **2**, and **3**, respectively. Thus, the DFT-PBE NMR calculations also reproduce the experimental trend, where δ_{iso} decreases when moving from **1** to **3**. The 16*i* and 24*k* sites show clearly larger theoretical δ_{iso} values. Since the experimental ^{27}Al NMR spectra show rather broad signals for these sites, the computational NMR results facilitate the interpretation of the 16*i* and 24*k* sites in the NMR spectra. In the case of **1**, the experimental spectrum shows two separate signals located at 315 and 275 ppm (difference of 40 ppm). The calculated δ_{iso} for 16*i* and 24*k* are 320 and 262 ppm, respectively (difference of 58 ppm between 16*i* and 24*k*). In the case of **2**, where the two signals overlap and produce a broad signal at 278 ppm, the calculated δ_{iso} for 16*i* and 24*k* are 273 and 244 ppm, respectively (difference of 29 ppm between 16*i* and 24*k*). Finally, for **3**, the calculated δ_{iso} corresponding to the broad experimental signal at 269 ppm are 244 and 257 ppm for 16*i* and 24*k*, respectively (difference of 13 ppm between 16*i* and 24*k*, but the ordering of is reversed in comparison to **1** and **2**). In summary, the calculated δ_{iso} reproduce the experimentally observed trend where the difference between 16*i* and 24*k* decreases when moving from **1** to **3** and the average δ_{iso} of the 16*i*+24*k* signal drifts towards the 6*c* signal. The above assignment of the ^{27}Al NMR spectrum is also in line with the quadrupolar coupling constants (C_q) calculated from the Electric Field Gradient (EFG) tensor (with absolute values of C_q averaged within each crystallographic site similar to δ_{iso}). For all structures **1**–**3**, the atoms at the most symmetric 6*c* position show smaller quadrupolar coupling values in comparison to the atoms at the less symmetric 16*i* and 24*k* positions, in agreement with previous studies on the $Ba_8Al_{14}Si_{31}$ clathrate.[26, 28] For example, in the case of **1**, the average C_q values for the 6*c*, 16*i*, and 24*k* positions are 1.2, 2.0, and 2.2 MHz, respectively.

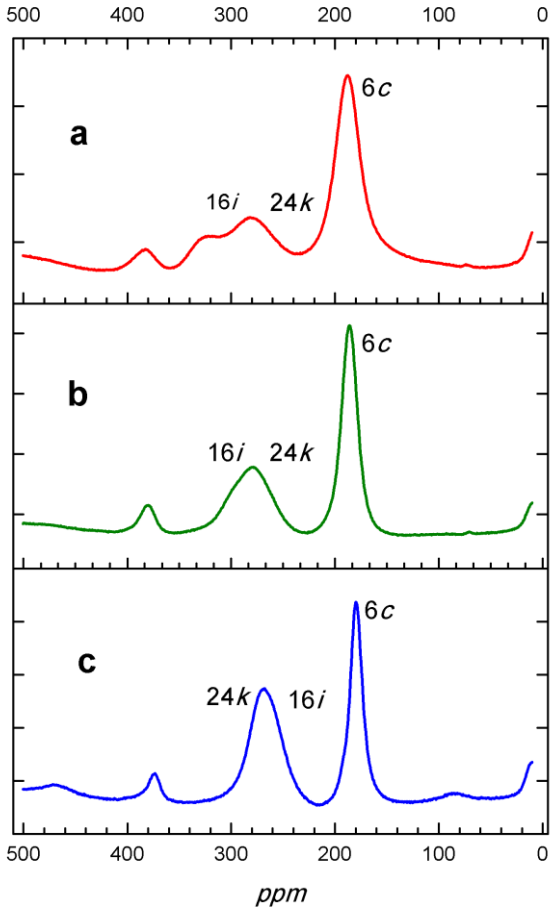

Figure 3. Part of the ^{27}Al MAS NMR spectra of $K_8Al_8Si_{38}$ (a), $Rb_8Al_8Si_{38}$ (b) and $C_{7.9}Al_{7.9}Si_{38.1}$ (c) at the rotating frequency of 15 kHz.

Thermoelectric transport properties were measured in the temperature range between 2 and 400 K. The temperature dependent electrical resistivity measurements (Figure 4a) of the compacted powder samples of **1** to **3** display semiconducting behavior. Magnetic measurements are in line with diamagnetic behavior of both compounds **1** and **2** (χ_{mol} = -6.47×10^{-4} emu×mol^{-1} and -6.70×10^{-4} emu×mol^{-1}, respectively, at room temperature.) and the presence of a small temperature independent paramagnetic contribution in compound **3** (1.27×10^{-3} emu×mol^{-1}, Figure S5).

The DFT-PBE band gaps of **1**, **2,** and **3** are 0.67, 0.74, and 0.79 eV, respectively, showing a slight increase from **1** to **3 (**it should be noted that band gaps are typically somewhat underestimated at the DFT-PBE level of theory).[33] The increase in the band gaps from **1** to **3** is in line with the resistivity values, which increase at room temperature as 0.64 Ωcm, 3.2 Ωm, and 540 Ωm for **1**, **2**, and **3**, respectively (Figure 4a). The dramatic change of resistivity behavior in **2** to **3** by more than a factor of 150 cannot be simply explained by the calculated increase of the corresponding band gaps by just 0.05 eV. Indeed, a careful inspection of the temperature dependence of the resistivity **2**, reveals that the resistivity behavior follows a (d = 3) three-dimensional variable range hopping (VRH) behavior according to formula (1):

$$\rho\ T\ = \rho_0 e^{(T_0\ T)^n};\quad n = \ d + 1 \qquad (1)$$

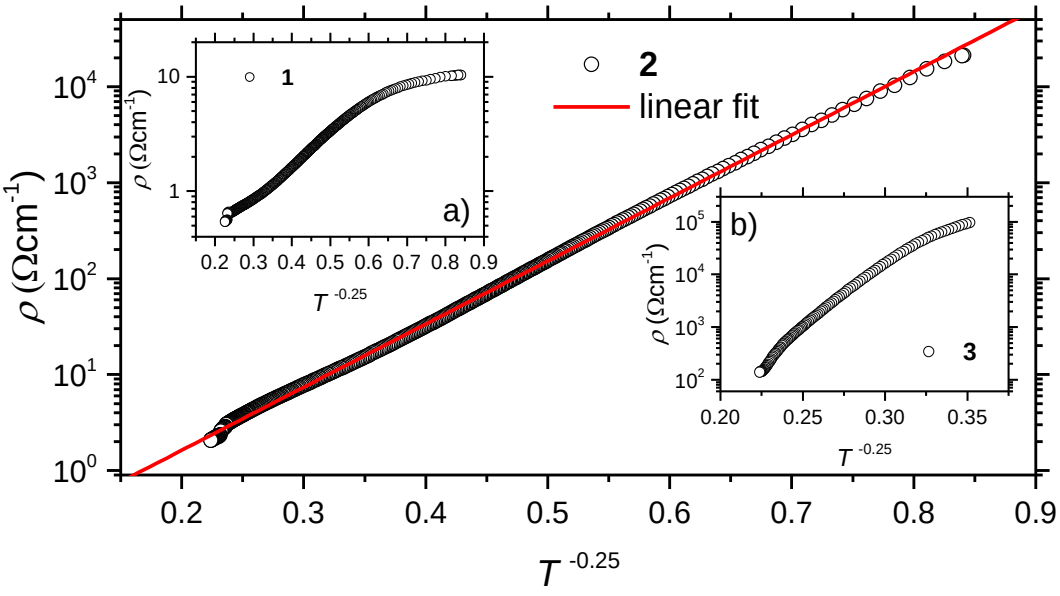

Figure 4. log(ρ) over $T^{-0.25}$ representation of the resistivity for **1** (inset a), **2** and **3** (inset b). The red line corresponds to a linear fit in agreement with variable range hopping behavior.

VRH behavior is commonly known to occur in disordered or amorphous semiconductors[34] at low temperatures and has already been observed in other clathrate species such as $K_8Ga_8Si_{38}$[35] or various Type I Sn clathrates[35-36] characterized by the presence of mixed occupancy sites. In case of **2** the $\rho(T)$ fit (1) yields a T_0 value of 5.24 * 10^5 K. This value is of similar magnitude compared to the one in $K_8Ga_8Si_{38}$ (T_0 = 1.24 * 10^5 K) which also displays a mixed occupancy of the 6*c* and ~~16i~~24*k* Wyckoff positions (see Table 7). We further note, that VRH in **2** is not limited to the low temperature regime alone, but extends up to room temperature, see Fig. 5. For **1**, however, the resistivity behavior can neither be described by VRH (see Fig. 4 inset a), nor by a purely semiconducting behavior (no linear relationship in an Arrhenius-type plot of the temperature dependent resistivity data), which might be caused by the noticeable Si and $Al_{1-x}Si_x$ impurities. For **3**, the low temperature resistivity data could not be reliably determined due to the high absolute ρ (T) values which were exceeding the dynamic range of the PPMS instrument employed.

The Seebeck coefficients *S* at room temperature (-222 µV/K for **1**, -252 µV/K for **2** and -300 µV/K for **3**) increase from **1** to **3** and are significantly higher than for example known Ba-Al-Si clathrates at room temperature: $Ba_8Al_{14}Si_{31}$ -21 µV/K,[18d] $Ba_{7.3}Sr_{0.3}Al_{14}Si_{31}$ shows -32 µV/K, [37] arc melted $Ba_8Al_{16}Si_{30}$ ≈ -48 µV/K.[38] The negative sign of these values is in agreement with other previously reported silicide-based clathrates and indicates that in these cases electrons are ~~representing~~ the predominant charge carriers. Accordingly, the majority of aluminum-silicide clathrates can be classified as n-type semiconductors.

We note, that the low temperature data of the Seebeck coefficients of **1**-**3** were noisy and have been discarded. Furthermore, we noticed that the temperature dependence of the Seebeck coefficient cannot be explained by a simple Mott-type (linear) contribution from the diffusion of charge carriers. On the other hand, variable range hopping is known to contribute to the Seebeck coefficient as well;[39] see equation (2):

$$S_{\mathrm{VRH}} \sim T^{\frac{(d-1)}{(d+1)}} \qquad (2)$$

Since the temperature dependent resistivity of **2** can be modeled by d = 3 VRH behavior, the same value for d has been assumed in the following to determine the Seebeck coefficient. Accordingly, the Seebeck coefficient of **1** and **2** has therefore been fitted by a linear combination of a diffusion part (~T) and a VRH part (~$T^{0.5}$) in equation (3):

$$S = AT + BT^{0.5} \qquad (3)$$

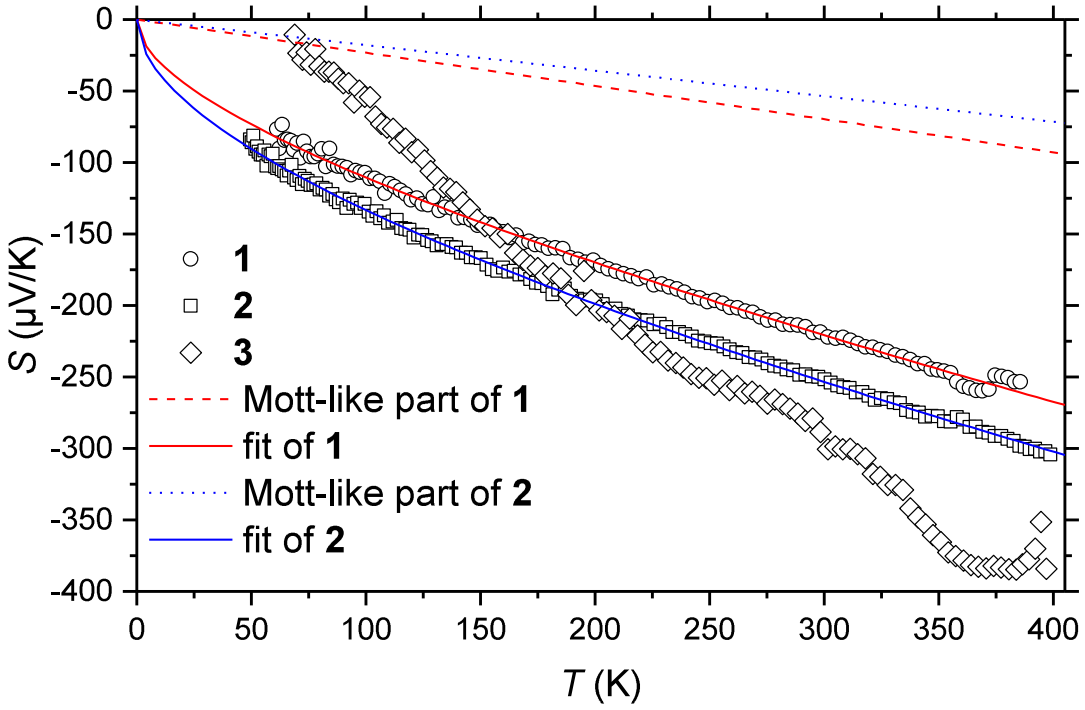

Figure 5. Temperature dependence of the Seebeck coefficient, S(T), of **1, 2** and **3**; fits according to equation 3 are marked by solid lines while and the individual Mott-type diffusion contribution in **1** and **2** are shown by dashed lines.

The same approach had been successfully used to describe the temperature dependence of the Seebeck coefficient for $Ba_8Ga_{16+x}Sb_xGe_{30-2x}$.[35a] Application of equation (3) in case of **1** and **2** (see Figure 5 and the Supporting Information Table S7) reveals, that the main contribution to the Seebeck coefficient originates from the VRH contribution and increases from **1** to **2**, whereas the linear diffusion contribution decreases from **1** (35% of the overall S-value) to **2** (24% of the overall S-value). The Seebeck coefficient of compound **3** shows a more complex temperature behavior and its origin is unknown.

The thermal conductivities at room temperature are 1.65 $Wm^{-1}K^{-1}$, 1.24 $Wm^{-1}K^{-1}$ and 0.93 $Wm^{-1}K^{-1}$ for **1**, **2** and **3**, respectively, are in the typical rage observed for other clathrates such as $Ba_8Al_xSi_{46-x}$[40] or $Ba_8Ga_{16}Ge_{30}$.[41] Due to the high resistivity, even for the sample **1**, the electronic contribution to the thermal conductivity is essentially zero. Therefore the total thermal conductivity equals the lattice conductivity. The values decreases with increasing size of the respective alkaline metal radius. The rattling of the guest atoms cannot explain this trend, because the rattling actually decreases with increasing mass and radii of the guest

atom, as evident by the crystallographic ADP analysis. However noticeable differences in the thermal conductivity have been attributed before to different arrangements of the framework atoms in $Ba_8Al_{16}Ge_{30}$.[18a]

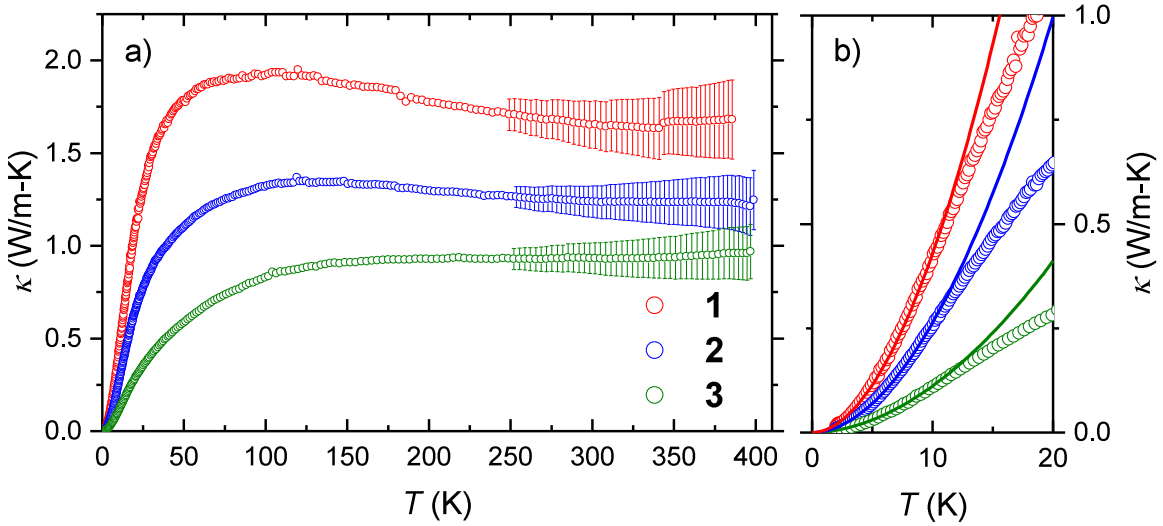

Figure 6. a) Thermal conductivity, $\kappa(T)$, of **1**, **2** and **3** from 2 to 400K. Error bars are shown for data above 250K. b) Low temperature behavior from 2 to 20 K. Solid lines correspond to power law fits ($A*T^B$) from 2 to 10K with exponents B = 1.88, 1.92 and 1.91 for **1**, **2** and **3** respectively.

Furthermore, we note in case of **1** (and **2**) the presence of a subtle local maximum at approx. T = 100K (Figure 6a), which is usually attributed to the degree of sample crystallinity. Such maxima typically occur when the samples' average crystallite size is significantly larger than the mean free path length of the phonons. In that case, the maximum reflects the onset of Umklapp-processes. For very pure and defect-free materials like diamond the magnitude at the maximum can exceed the room temperature value by several orders of magnitude. Due to the compacting of the samples at pressures of 4GPa without annealing at elevated temperatures, the crystallite size will be very small and thus the maximum of the thermal conductivity is only slightly higher than the room temperature value. For **2** the maximum is even less pronounced and for **3** there is no maximum at all. The low temperature thermal conductivity (below 10K) displays a T^2 behavior for all samples (Figure 6b), which is known for glass like materials as well as other clathrates such as $Sr_8Ga_{16}Ge_{30}$[42] or $Ba_8Ga_{16}Ge_{30}$.[41, 43]

Despite the presence of a rather high Seebeck coefficient, which increases from **1** to **3**, and a low thermal conductivity, which decreases from **1** to **3**, the figure of merit ZT (Figure 7) at 350 K is very low and decreases from **1** to **3** due to the increasing electrical resistivity of **1**-**3**. ZT values at 350 K are 2×10^{-2} for $K_8Al_8Si_{38}$, 9×10^{-4} for $Rb_8Al_8Si_{38}$ and 2×10^{-5} for $C_{7.9}Al_{7.9}Si_{38.1}$. However, lowering the temperature dependent resistivity behavior of **1**-**3** by controlling the samples' grain size or optimizing the doping strategy, might render these clathrates into promising materials suitable for thermoelectrical applications.

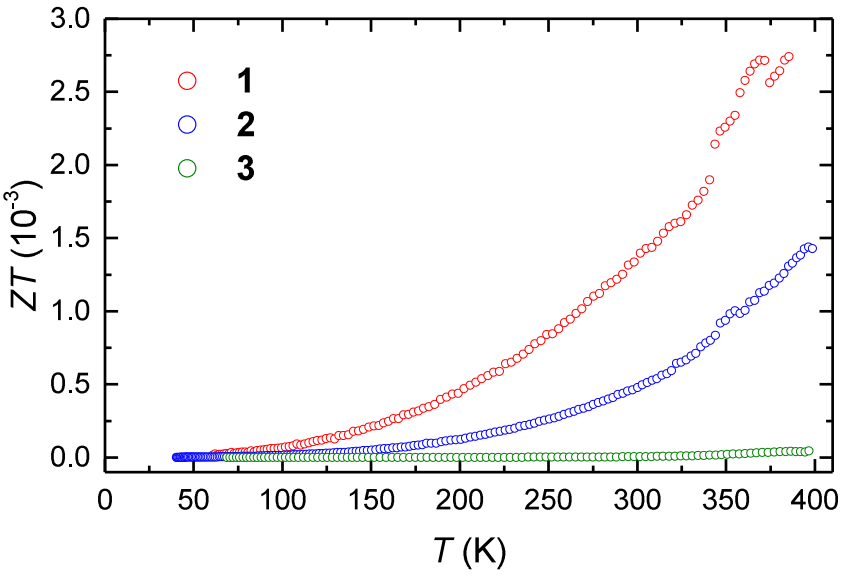

Figure 7. Thermoelectric figure of merit *ZT* of samples for **1**, **2** and **3** respectively

Discussion

Table 7 summarizes known ternary intermetallic clathrate-I compounds formed by alkali metals, triel, and tetrel elements. For most of known structures a mixed occupancy at all host atom positions 6*c*, 16*i* and 24*k* is observed. The here reported compounds **1** to **3** follow the same trend. The diamagnetic behavior with negative susceptibility values for **1** and **2** as well as the temperature independent susceptibility, however with a small positive value for **3** hint for all three compounds being electron precise Zintl phases of the composition $A_8Tr_8Tt_{38}$ ($A_{8-x}Tr_{8-x}Tt_{38+x}$ in case of compound **3**). Due to the novel synthetic route the compounds are obtained in sufficient quantities to perform neutron diffraction experiments on powdered samples of **1** to **3**. The results of the Rietveld structure refinement are shown in Table 2 and 4. For compounds **2** ~~and **3**~~ the free refinement of the ~~side~~ site occupations factors resulted in the values expected for the diamagnetic compounds $A_8Tr_8Tt_{38}$. Since for compound **1** the refinement did not converge the composition was fixed also to the electron precise composition $K_8Al_8Si_{38}$ of a Zintl phase due to its clear diamagnetic behavior. The atomic positions of both guest atoms 2*a* and 6*d* are for compounds **1** and **2** fully occupied. In case of the semiconducting compound **3** a small Cs deficiency (approx. 5% at 2*a* atomic site) hints for fixing the composition to the electron precise composition $C_{7.9}Al_{7.9}Si_{38.1}$. For Al and Si atoms mix on all framework atom positions, but Al is clearly preferred at 6*c* positions. Same trends are observed for all other representative clathrates of group III and IV elements as given in Table 7 whose structures have been well refined. In the case of Al and Si this trend is understandable since the larger Al atoms preferentially occupy positions that are major part of the six-membered ring of the larger cage of the clathrate structure also having larger distances to the centering alkali metal atoms. This observation is supported by the decreasing Al content at the 6c position (and thus increasing content on 16i and 24k) with increasing size of alkali metal guest atom K, Rb, and Cs in compounds **1** to **3**.

Table 7. Occupancies for clathrates with composition $A_8(Tr)_8(Tt)_{38}$ (III=Al, Ga, In; VI=Si, Ge, Sn)

	Tr	*Tt*	*Tr*	*Tt*	*Tr*	*Tt*
		6c		***16i***		***24k***
$K_8Al_{8.02(9)}Si_{37.98(9)}$ [a]	0.75(3)	0.25(3)	0.04(1)	0.96(1)	0.12(1)	0.88(1)
$Rb_8Al_{8.01(17)}Si_{37.99(17)}$ [b]	0.60(4)	0.40(4)	0.05(3)	0.95(3)	0.15(2)	0.85(2)
$Cs_{7.89(1)}Al_{7.90(11)}Si_{38.10(11)}$ [a]	0.41(3)	0.59(3)	0.10(2)	0.90(2)	0.16(1)	0.84(1)
$K_8Ga_{7.90(4)}Si_{38.10(4)}$ [35] [f]	0.566(2)	0.434(2)	0.175(7)	0.825(7)	0.019(6)	0.981(6)
$Rb_8Ga_{7.93(5)}Si_{38.07(5)}$ [44] [c]	0.409(5)	0.591(5)	0.220(7)	0.780(7)	0.012(9)	0.988(9)
$K_8Al_{7.96(6)}Ge_{38.04(6)}$ [45] [c]	0.822(4)	0.178(4)	0.08(1)	0.92(1)	0.069(6)	0.931(6)
$Rb_8Al_{7.84(7)}Ge_{38.16(7)}$ [46] [c]	0.92(2)	0.08(2)	0.07(1)	0.93(1)	0.04(1)	0.96(1)
$Rb_8Ga_8Ge_{38}$ [44] [d]	0.174	0.826	0.174	0.826	0.174	0.826
$Cs_8Ga_8Ge_{38}$ [47] [d]	0.174	0.826	0.174	0.826	0.174	0.826
$K_8In_{8.14(7)}Ge_{37.86(7)}$ [48][c]	0.93(1)	0.07(1)	0.08(1)	0.92(1)	0.04(1)	0.96(1)
$Rb_8In_{7.82(7}Ge_{38.18(7)}$ [48] [c]	0.89(1)	0.11(1)	0.09(1)	0.91(1)	0.02(1)	0.98(1)
$Cs_8In_{8.22(12)}Ge_{37.78(12)}$ [49] [f]	0.77(3)	0.23(3)	0.15(2)	0.85(2)	0	1
$K_8Al_8Sn_{38}$ [45] [c]	0.12	0.88	0.28	0.72	0.05	0.95
$Rb_8Al_8Sn_{38}$ [46] [c]	0.11	0.89	0.37	0.63	0.10	0.90
$K_8Ga_{8.1(1.3)}Sn_{37.9(1.3)}$ [50] [f]	0.54	0.46	0.09	0.91	0.17	0.83
$Rb_8Ga_8Sn_{38}$ [44] [c]	0.549	0.451	0.15	0.85	0.08	0.92
$Cs_8Ga_8Sn_{38}$ [47] [c]	0.484	0.516	0.158	0.842	0.075	0.925

[a] Refined of occupancy parameters with fixed composition from neutron powder data
[b] Free refinement of all occupancy parameters from neutron powder data
[c] Refinement with a statistical occupation parameters of the framework from X-ray single crystal data
[d] Refined with fixed occupancy parameters from X-ray single crystal data
[f] Free refinement of all occupancy parameters from X-ray single crystal data

Conclusion

We reported a novel, easy to scale-up synthetic route of three Si-based intermetallic clathrates with composition $K_8Al_8Si_{38}$, $Rb_8Al_8Si_{38}$ and $C_{7.9}Al_{7.9}Si_{38.1}$. The synthesis route allows the production of pure phase samples with relatively high yields. The crystal structures of the three clathrates were refined from neutron powder data using the Rietveld methods well as from X-ray diffraction data. The site occupation factors of Si and Al on the host atom sites are consistent with our results from ^{27}Al-MAS NMR spectroscopic data. Transport property measurements in temperature range from 2 till 400 K reveal a decrease of the values for thermal conductivity and an increase of the Seebeck coefficient as well as resistivity values from K to Cs. The behavior of the electrical resistivity as well as the Seebeck coefficient can be partially interpreted by a variable range hopping. Even the clathrates show high values of Seebeck coefficient, relatively high resistivity values lead to small figure of merits ZT decreasing from K to Cs.

Experimental Section

Syntheses

All synthesis steps were performed in Ar filled glove box with levels of O_2 and H_2O less than 1 ppm. Clathrates **1**, **2** and **3** were prepared from pure elements K (ampoule, 99%), Rb (ampoule, 99.6%, Aldrich), Cs (ampoule, 99.98%, ABCR), Al (granules 2-10 mm, 99.99%, Chempur) and Si (chips, 99.9999%, ABCR). As a preliminary step, Al and Si were arc melted (atomic ratio 1:1) and subsequently ground by ball-milling into a fine powder. The resulting Al/Si powder (0.6048 g for clathrate **1**, 0.5888 g for **2** and 0.4937 g for **3)** were mixed with approximately 0.5-0.8 g of the respective alkali-metal halide salt KBr (>99.5%, Emsure), RbCl (99%, Alfa Aesar) and CsCl (>99.9%, VWR) in a mortar. The mixtures and alkali metals (0.098g K, 0.2086 g Rb, and 0.2719 g Cs, respectively) were placed in alumina crucibles (Al_2O_3, D8×5×50, FRIATEC AG), which then were sealed in niobium ampoules and placed in silica protection jackets. The samples were heated in a muffle furnace. The excess Al and the alkali metal halide salt serve as a flux medium.[51] Heating to 1173 K was performed at a rate of 1 K/min. After 1 h of tempering at this temperature the samples were cooled to 923 K at a rate of 0.3 K/min, and further to room temperature at 1 K/min.

After the reaction the halide salts and the phase *A*Si (*A*=K, Rb, Cs) were removed from the reaction mixture by treating the alumina crucible containing the product with 60 ml of distilled water at 80° C in an ultrasonic bath. The sample was subsequently washed several times with aliquots of 60 ml of distilled water. Afterwards the excess of Al was dissolved using 50 ml of 1 M HCl solutions at 80° C in an ultrasonic bath and to remove elemental Si the residue was finally treated using 50 ml of 1 M NaOH under the same conditions otherwise. In the final step the sample was additionally washed several times with water and subsequently with acetone and the residue dried at 120 °C over 12h. After all cleaning procedures the yield was 30% to 60 % for the various samples based on Al/Si (0.3 – 0.6 g). The product is a crystalline powder with metallic luster. Clathrates **1**, **2** and **3** are stable towards air and moisture.

Powder X-ray diffraction (PXRD)

Powder X-ray diffraction (PXRD) data were collected with a Stoe STADI P powder diffractometer with linear position sensitive detector and Cu *Kα* radiation (λ=1.5406 Å). The sample was ground to the fine powder and filled into glass capillaries (0.3 mm diameter Mark-Röhrchen). Data were collected for rotating samples from 10° to 90° (2θ). Al_2O_3 was used as an external standard to get precise values of the unit cell parameters. Powder

patterns were indexed by the WinPLOTR[52] package. As an example the diffractogram together with the Rietveld fit is shown in Figure 1 for compound **1**.

Neutron powder diffraction (NPD)

Neutron powder measurements were performed for 3, 4 and 5 g of clathrates **1**, **2** and **3**, respectively. Besides Si and $Al_{1-x}Si_x$ as minor phases (4.50% and 6.28%, respectively), the sample with clathrate **1** showed to be the main phase (according to X-ray powder patterns). Clathrates **2** and **3** samples contain $Al_{1-x}Si_x$ as impurity: 2.13 % and 0.71%, correspondingly. The neutron scattering experiments were performed on the high-resolution powder diffractometer SPODI at the research reactor FRM-II (Garching, Germany). Monochromatic neutrons (λ=1.5482 Å) were obtained at a 160° take-off angle using the (551) reflection of a vertically focused composite Ge monochromator. The vertical position sensitive multidetector (300 mm effective height) consisting of 80 ^{3}He tubes and covering an angular range of 160º in 2θ was used for data collection. Measurements were performed in Debye–Scherrer geometry. The powder sample was filled into a thin-wall (0.15 mm) vanadium can of 14 mm in diameter.

The Rietveld refinement was carried out using the FullProf[52] package. The peak profile shape was described by a pseudo-Voigt function. For clathrates **2** and **3** the background of the diffraction pattern was fitted using a 6-coefficient polynomial function. For the clathrate **1** the background was fitted using a linear interpolation between selected data points in non-overlapping regions. The absorption correction coefficient (μ_R) was calculated using http://www.ncnr.nist.gov/instruments/bt1/neutron.html.

The scale factor, lattice parameter, fractional coordinates of atomic sites, zero angular shift and profile shape parameters, isotropic displacement parameters and site occupancies were varied during the fitting procedure. Relevant crystallographic and refinement data are listed in Table 2.

Single crystal X-ray diffraction measurements

Single crystals of different sizes were picked from the reaction products. Crystals of excellent quality were carefully selected for the further studies. X-ray single crystal data were collected on a Bruker APEX II diffractometer equipped with a CCD detector, a Ge monochromator and Mo K_α radiation (λ = 0.71073 Å). The frames were integrated with the Bruker SAINT[53] software package using a narrow-frame algorithm. Data were corrected for absorption effects using the numerical absorption method (SADABS[54]). The structure refinements using an independent atom model were performed using SHELXL 97.[55] The refinement was performed with the full-matrix least squares on F^2. The thermal motion of all atoms was refined anisotropically during the initial refinements. The structure models obtained from neutron powder measurement were applied to the refinements of the present structures. Details of the refinement are given in Table 3.

For clathrates **1** to **3** also single crystal X-ray data were used for the refinement of the structure parameters. For compound **1** all parameters including the Al : Si ratios on all positions were independently refined. For **2** and **3** the refinement of the Al : Si ratio converged for the 6*c* and 24*k* positions but not for 16*i*. Therefore the Al/Si ratio as obtained from the neutron diffraction data was applied. For **3** chemical restrains (fixed Al/Si ratio) were included to determine the Cs1 occupation factor: The Al:Si ratio was fixed to 8:38 as for clathrate **1** or alternatively the Al content was adapted accordingly to the Cs content to get an electron precise valence compound (Cs:Al:Si = 7.9:7.9:38.1). After applying the restrain it was possible to refine the occupancy of 2*a* site and the distribution of Al on the various positions of the structure. Both models resulted virtually with the same values $Cs_{7.9}Al_8Si_{38}$ and $Cs_{7.9}Al_{7.9}Si_{38.1}$, respectively The resistivity measurement clearly indicated the semiconducting nature of clathrate **3**.

The lattice parameter determined from the X-Ray powder diffraction data (Table 1) were used throughout for the refinement of the single crystal data. Further details on the structure refinement may be obtained from: Fachinformationszentrum Karlsruhe, D–76344 Eggenstein-Leopoldshafen (Germany), by quoting the depository numbers CSD-427684 (**1**), CSD-427685 (**2**), and CSD-427686 (**3**).

Energy Dispersive X-ray Spectroscopy (EDX)

To determine the composition of clathrates **1** to **3** we used a JEOL-JSM 7500F scanning electron microscope equipped with and an Oxford X-Max EDX analyzer with Mn as internal standard. Data was collected from different parts of the crystal and minimum for two representative crystals of each compound.

Magnetic Measurements

The measurements for **1** to **3** were performed with a SQUID magnetometer (Quantum Design MPMS XL-5). The polycrystalline sample (42 mg of **1**, 57 mg of **2** and 65 mg of **3**) was first zero-field cooled to 2 K and checked for superconductivity at a field of 0.01 Tesla. Magnetic susceptibility was measured in the temperature range from 2 to 300 K at a field of 3 Tesla.

Solid state NMR

^{27}Al MAS NMR measurements were obtained by using a Bruker Avance 300 MHz spectrometer.^{27}Al MAS NMR measurements (resonance frequency of 78.276 MHz) were performed in 4 mm ZrO_2 rotors at a spinning speed of 10 and 15 kHz respectively with 1000 up to 10.000 scans, and single pulse technique with a pulse length of 3 μs and a repetition time of 2 s. The integration to determine the peak's intensity was performed with OriginPro program[56] considering the background as a linear interpolation between selected points.

Computational details

First-principles density functional theory (DFT) calculations were carried out with the CASTEP program package[57] using the PBE exchange-correlation functional[58] and ultrasoft pseudopotentials generated with the on-the-fly scheme.[59] Plane-wave basis set cut-offs of 500 eV, 270 eV, and 240 eV were applied for the structures **1**, **2**, and **3**, respectively (K and Rb pseudopotentials required higher cut-offs in comparison to Cs, Si, and Al). 3x3x3 Monkhorst-Pack sampling was used for integrations in the reciprocal space, corresponding to a *k*-point grid spacing of approximately 0.03 Å^{-1}.[60] The isotropic chemical shielding (σ_{iso}) and Electric Field Gradient (EFG) tensors for ^{27}Al were obtained using the GIPAW formalism as implemented in CASTEP-NMR.[61] The ^{27}Al chemical shifts (δ_{iso}) were evaluated with respect to aqueous Al^{3+} ion described as $[Al(H_2O)_6]^{3+}$ (σ_{ref} = 561.2 ppm). The calculations for the molecular $[Al(H_2O)_6]^{3+}$ reference system were carried out in a primitive cubic cell (a = 15 Å) using a plane-wave basis set cut-off of 610 eV and one *k*-point.

Transport measurements

Fine grounded samples have been compacted at 4GPa in a High Pressure Multi-Anvil apparatus. The pressure was reached at about 1GPa/h, kept for 1 hour and then released at the same rate. Samples of approx. density of 96% have been recovered as round cylinders with a length of approx. 7 mm and a diameter of 4.5 mm. The density of samples was measured using the gas displacement pycnometer AccuPyc 1330. The purity of all samples was checked by powder X-ray diffraction before and after pressing. No changes occurred. The samples were finally cut into bars with dimensions of 7×2×3mm for measurements on a Physical Properties Measurement System (PPMS) using the Thermal Transport Option (TTO). Au-coated copper leads have been glued to the sample via silver-filled epoxy EpoTek H31E. The measurements were performed in high vacuum (10^{-6} bar) using the Thermal Transport Option (TTO) of the PPMS. The measurement was taken in continuous measurement mode with a slope of 0.5 K min^{-1}. The equilibrium temperature difference was obtained from

extrapolation via a fit to the response of a heat pulse. Radiation heat losses were automatically corrected by the incorporated software of the PPMS system. The auto range feature was used for all of the measurements carried out in the PPMS system. For precise resistivity measurements smaller samples (4x0.5x1mm) have been used that were contacted to 0.05mm Pt-wires via silver paint.

Acknowledgment

This work has been funded by the Deutsche Forschungsgemeinschaft Project No. FA 198/11-1. A. J. K. gratefully acknowledges funding from the Academy of Finland (grant 138560/2010) and the Foundation for Research of Natural Resources in Finland. The computing resources for this work were provided by the Finnish IT Center for Science (CSC).

References

[1] J. S. Kasper, P. Hagenmul, M. Pouchard, C. Cros, *Science* **1965**, *150*, 1713.

[2] a) F. J. DiSalvo, *Science* **1999**, *285*, 703-706; b) G. S. Nolas, J. Poon, M. Kanatzidis, *Mrs Bulletin* **2006**, *31*, 199-205.

[3] A. Saramat, G. Svensson, A. E. C. Palmqvist, C. Stiewe, E. Mueller, D. Platzek, S. G. K. Williams, D. M. Rowe, J. D. Bryan, G. D. Stucky, *J. Appl. Phys* **2006**, *99*.

[4] E. S. Toberer, M. Christensen, B. B. Iversen, G. J. Snyder, *Phys. Rev. B* **2008**, *77*.

[5] Y. Saiga, B. Du, S. K. Deng, K. Kajisa, T. Takabatake, *J. Alloys Compd.* **2012**, *537*, 303-307.

[6] A. V. Shevelkov, K. Kovnir, in *Zintl Phases: Principles and Recent Developments, Vol. 139* (Ed.: T. F. Fassler), Springer-Verlag Berlin, Berlin, **2011**, pp. 97-142.

[7] A. J. Karttunen, T. F. Fässler, M. Linnolahti, T. A. Pakkanen, *Inorg. Chem.* **2011**, *50*, 1733-1742.

[8] a) F. Dubois, T. F. Fassler, *J. Am. Chem. Soc.* **2005**, *127*, 3264-3265; b) A. Kaltzoglou, S. D. Hoffmann, T. F. Fässler, *Eur. J. Inorg. Chem.* **2007**, 4162-4167; c) A. Kaltzoglou, T. Fässler, M. Christensen, S. Johnsen, B. Iversen, I. Presniakov, A. Sobolev, A. Shevelkov, *J. Mater. Chem.* **2008**, *18*, 5630-5637.

[9] V. L. Kuznetsov, L. A. Kuznetsova, A. E. Kaliazin, D. M. Rowe, *J. Appl. Phys.* **2000**, *87*, 7871-7875.

[10] W. Jung, J. Loerincz, R. Ramlau, H. Borrmann, Y. Prots, F. Haarmann, W. Schnelle, U. Burkhardt, M. Baitinger, Y. Grin, *Angew. Chem. Int. Ed.* **2007**, *46*, 6725-6728.

[11] L. Yang, Y. Wang, T. Liu, T. D. Hu, B. X. Li, K. Stahl, S. Y. Chen, M. Y. Li, P. Shen, G. L. Lu, Y. W. Wang, J. Z. Jiang, *J. Solid State Chem.* **2005**, *178*, 1773-1777.

[12] G. Cordier, P. Woll, *J. Less-Common Met.* **1991**, *169*, 291-302.

[13] a) H. G. von Schnering, M. Somer, M. Kaupp, W. Carrillo-Cabrera, M. Baitinger, A. Schmeding, Y. Grin, *Angew. Chem. Int. Ed.* **1998**, *37*, 2359-2361; b) R. Schafer, W. Klemm, *Z. Anorg. Allg. Chem.* **1961**, *312*, 214-220.

[14] T. Rachi, K. Tanigaki, R. Kumashiro, J. Winter, H. Kuzmany, *Chem. Phys. Lett.* **2005**, *409*, 48-51.

[15] S. Stefanoski, M. Beekman, W. Wong-Ng, P. Zavalij, G. S. Nolas, *Chem. Mater.* **2011**, *23*, 1491-1495.

[16] A. Wosylus, I. Veremchuk, W. Schnelle, M. Baitinger, U. Schwarz, Y. Grin, *Chem. Eur. J.* **2009**, *15*, 5901-5903.

[17] a) M. Omori, *Mater. Sci. Eng. A* **2000**, *287*, 183-188; b) M. Beekman, M. Baitinger, H. Borrmann, W. Schnelle, K. Meier, G. S. Nolas, Y. Grin, *J. Am. Chem. Soc.* **2009**, *131*, 9642-9643; c) K. Akai, T. Uemura, K. Kishimoto, T. Tanaka, H. Kurisu, S. Yamamoto, T. Koyanagi, K. Koga, H. Anno, M. Matsuura, *J. Electron. Mater.* **2009**, *38*, 1412-1417; d) M. Hayashi, K. Kishimoto, K. Kishio, K. Akai, H. Asada, T. Koyanagi, *Dalton Trans.* **2010**, *39*, 1113-1117.

[18] a) M. Christensen, B. B. Iversen, *Chem. Mater.* **2007**, *19*, 4896-4905; b) C. L. Condron, S. M. Kauzlarich, T. Ikeda, G. J. Snyder, F. Haarmann, P. Jeglic, *Inorg. Chem.* **2008**, *47*, 8204-8212; c) C. L. Condron, R. Porter, T. Guo, S. M. Kauzlarich, *Inorg. Chem.* **2005**, *44*, 9185-9191; d) C. L. Condron, J. Martin, G. S. Nolas, P. M. B. Piccoli, A. J. Schultz, S. M. Kauzlarich, *Inorg. Chem.* **2006**, *45*, 9381-9386.

[19] B. Boehme, U. Aydemir, A. Ormeci, W. Schnelle, M. Baitinger, Y. Grin, *Sci. Technol. Adv. Mater.* **2007**, *8*, 410-415.

[20] B. Boehme, A. Guloy, Z. Tang, W. Schnelle, U. Burkhardt, M. Baitinger, Y. Grin, *J. Am. Chem. Soc.* **2007**, *129*, 5348–5349.

[21] a) N. Melnychenko-Koblyuk, A. Grytsiv, P. Rogl, M. Rotter, R. Lackner, E. Bauer, L. Fornasari, F. Marabelli, G. Giester, *Phys. Rev. B* **2007**, *76*, 195124; b) N. Melnychenko-Koblyuk, A. Grytsiv, P. Rogl, M. Rotter, E. Bauer, G. Durand, H. Kaldarar, R. Lackner, H. Michor, E. Royanian, M. Koza, G. Giester, *Phys. Rev. B* **2007**, *76*, 144118; c) N. L. Okamoto, M. W. Oh, T. Nishii, K. Tanaka, H. Inui, *J. Appl. Phys.* **2006**, *99*, 033513.

[22] A. Kaltzoglou, S. Ponou, T. F. Fässler, *Eur. J. Inorg. Chem.* **2008**, 4507-4510.

[23] a) A. Kaltzoglou, S. Ponou, T. F. Fässler, *Eur. J. Inorg. Chem.* **2008**, 538-542; b) A. P. Wilkinson, C. Lind, R. A. Young, S. D. Shastri, P. L. Lee, G. S. Nolas, *Chem. Mater.* **2002**, *14*, 1300-1305; c) G. S. Nolas, T. J. R. Weakley, J. L. Cohn, *Chem. Mater.* **1999**, *11*, 2470-2473.
[24] J. Rodriguez-Carvajal, *Physica B.* **1993**, *192*, 55-69.
[25] a) E. Zintl, *Angew. Chem.* **1939**, *52*, 1-6; b) H. Schafer, Eisenman.B, W. Muller, *Angew. Chem. Int. Ed.* **1973**, *12*, 694-712; c) W. Klemm, *Proceedings of the Chemical Society of London* **1958**, 329-341.
[26] R. Nesper, *Prog. Solid State Chem.* **1990**, *20*, 1-45.
[27] Y. He, F. Sui, S. M. Kauzlarich, G. Galli, *Energy Environ. Sci.* **2014**.
[28] P. Sheng, *Science* **1972**, *176*, 903-904.
[29] T. B. Massalski, M. J. L., B. L. H., B. H., *Binary alloy phase diagrams*, American Society for Metals, Metals Park, Ohio, **1986**.
[30] K. A. McLauchlan, *Nature* **1988**, *331*, 221-221.
[31] M. Christensen, S. Johnsen, B. B. Iversen, *Dalton Trans.* **2010**, *39*, 978-992.
[32] N. P. Blake, D. Bryan, S. Latturner, L. Mollnitz, G. D. Stucky, H. Metiu, *J. Chem. Phys.* **2001**, *114*, 10063-10074.
[33] Y. Imai, M. Imai, *J. Alloys Compd.* **2011**, *509*, 3924-3930.
[34] N. F. Mott, *Philos. Mag.* **1969**, *19*, 835-852.
[35] M. Imai, A. Sato, H. Udono, Y. Imai, H. Tajima, *Dalton Trans.* **2011**, *40*, 4045-4047.
[36] a) V. H. Tran, W. Muller, K. F. Cai, H. F. Wang, X. R. He, in *Thermoelectrics, 2006. ICT '06. 25th International Conference on*, **2006**, pp. 681-683; b) G. S. Nolas, J. L. Cohn, J. S. Dyck, C. Uher, J. Yang, *Phys. Rev. B* **2002**, *65*, 165201.
[37] C. L. Condron, S. M. Kauzlarich, *Inorg. Chem.* **2007**, *46*, 2556-2562.
[38] Y. Mudryk, P. Rogl, C. Paul, S. Berger, E. Bauer, G. Hilscher, C. Godart, H. Noel, *J. Phys.: Condens. Matter* **2002**, *14*, 7991-8004.
[39] I. P. Zvyagin, *Phys. Status Solidi B* **1973**, *58*, 443-449.
[40] a) H. Anno, M. Hokazono, R. Shirataki, Y. Nagami, *J Mater Sci* **2013**, *48*, 2846-2854; b) N. Tsujii, J. H. Roudebush, A. Zevalkink, C. A. Cox-Uvarov, G. Jeffery Snyder, S. M. Kauzlarich, *J. Solid State Chem.* **2011**, *184*, 1293-1303.
[41] L. Bertini, K. Billquist, D. Bryan, M. Christensen, C. Gatti, L. Holmgren, B. B. Iversen, E. Mueller, M. Muhammed, G. Noriega, A. E. C. Palmqvist, D. Platzek, D. M. Rowe, A. Saramat, C. Stiewe, G. D. Stucky, G. Svensson, M. Toprak, S. G. K. Williams, Y. Zhang, in *Thermoelectrics, 2003 Twenty-Second International Conference on - ICT*, **2003**, pp. 127-130.
[42] a) K. Umeo, M. A. Avila, T. Sakata, K. Suekuni, T. Takabatake, *J. Phys. Soc. Jpn.* **2005**, *74*, 2145-2148; b) G. S. Nolas, J. L. Cohn, G. A. Slack, S. B. Schujman, *Appl. Phys. Lett.* **1998**, *73*, 178-180.
[43] a) A. Bentien, M. Christensen, J. D. Bryan, A. Sanchez, S. Paschen, F. Steglich, G. D. Stucky, B. B. Iversen, *Phys. Rev. B* **2004**, *69*, 045107; b) M. Christensen, N. Lock, J. Overgaard, B. B. Iversen, *J. Am. Chem. Soc.* **2006**, *128*, 15657-15665.
[44] H. G. von Schnering, R. Kroner, H. Menke, K. Peters, R. Nesper, *Z. Kristallogr.–New Cryst. Struct.* **1998**, *213*, 677-678.
[45] R. Kroner, K. Peters, H. G. von Schnering, R. Nesper, *Z. Kristallogr.–New Cryst. Struct.* **1998**, *213*, 675-676.
[46] R. Kroner, K. Peters, H. G. von Schnering, R. Nesper, *Z. Kristallogr.–New Cryst. Struct.* **1998**, *213*, 669-670.
[47] R. Kroner, K. Peters, H. G. von Schnering, R. Nesper, *Z. Kristallogr.–New Cryst. Struct.* **1998**, *213*, 671-672.
[48] H. G. von Schnering, H. Menke, R. Kroner, E. M. Peters, K. Peters, R. Nesper, *Z. Kristallogr.–New Cryst. Struct.* **1998**, *213*, 673-674.
[49] H. Menke, W. Carrillo-Cabrera, K. Peters, E. M. Peters, H. G. von Schnering, *Z. Kristallogr.–New Cryst. Struct.* **1999**, *214*, 14-14.
[50] R. Kroner, K. Peters, H. G. von Schnering, R. Nesper, *Z. Kristallogr.–New Cryst. Struct.* **1998**, *213*, 667-668.

[51] Y. Liu, L.-M. Wu, L.-H. Li, S.-W. Du, J. D. Corbett, L. Chen, *Angew. Chem. Int. Ed.* **2009**, *48*, 5305-5308.
[52] J. R.-C. T. Roisnel, version 3.20 LLB.LCSIM ed., **2005**.
[53] Bruker, Bruker AXS Inc., Madison, Wisconsin, USA., **2001**.
[54] Bruker, in *SADABS*, Bruker AXS Inc., Madison, Wisconsin, USA., **2001**.
[55] G. M. Sheldrick, *Acta Crys.* **2008**, *A64*, 112-122.
[56] OriginLab, Northampton, MA.
[57] S. J. Clark, M. D. Segall, C. J. Pickard, P. J. Hasnip, M. J. Probert, K. Refson, M. C. Payne, *Z. Kristall.* **2005**, *220*, 567-570.
[58] J. P. Perdew, K. Burke, M. Ernzerhof, *Phys. Rev. Lett.* **1996**, *77*, 3865-3868.
[59] D. Vanderbilt, *Phys. Rev. B* **1990**, *41*, 7892-7895.
[60] H. J. Monkhorst, J. D. Pack, *Phys. Rev. B* **1976**, *13*, 5188-5192.
[61] a) C. J. Pickard, F. Mauri, *Phys. Rev. B* **2001**, *63*; b) J. R. Yates, C. J. Pickard, F. Mauri, *Phys. Rev. B* **2007**, *76*.